

# ATCA 16 cm observation of CIZA J1358.9–4750: Implication of merger stage and constraint on non-thermal properties

Takuya AKAHORI,<sup>1,2,\*</sup> Yuichi KATO,<sup>3</sup> Kazuhiro NAKAZAWA,<sup>3,4,5</sup>  
Takeaki OZAWA,<sup>1,6</sup> Liyi GU,<sup>7</sup> Motokazu TAKIZAWA,<sup>8</sup> Yutaka FUJITA,<sup>9</sup>  
Hiroyuki NAKANISHI,<sup>1</sup> Nobuhiro OKABE,<sup>10,11</sup> and Kazuo MAKISHIMA<sup>3,12</sup>

<sup>1</sup>Graduate School of Science and Engineering, Kagoshima University, 1-21-35 Korimoto, Kagoshima, Kagoshima 890-0065, Japan

<sup>2</sup>Mizusawa VLBI Observatory, National Astronomical Observatory Japan, 2-21-1 Osawa, Mitaka, Tokyo 181-8588, Japan

<sup>3</sup>Department of Physics, The University of Tokyo, 7-3-1 Hongo, Bunkyo-ku, Tokyo, 113-0033, Japan

<sup>4</sup>Center for Experimental Studies, Kobayashi-Maskawa Institute for the Origin of Particles and the Universe, Furo-cho, Chikusa-ku, Nagoya, Aichi 464-8602, Japan

<sup>5</sup>Division of Particle and Astrophysical Science, Graduate School of Science, Nagoya University, Furo-cho, Chikusa-ku, Nagoya, Aichi 464-8602, Japan

<sup>6</sup>Astronomical Data Center, National Astronomical Observatory of Japan, 2-21-1 Osawa, Mitaka, Tokyo 181-8588, Japan

<sup>7</sup>SRON Netherlands Institute for Space Research, Sorbonnelaan 2, 3584 CA Utrecht, the Netherlands

<sup>8</sup>Department of Physics, Yamagata University, 1-4-12 Kojirakawa-machi, Yamagata, Yamagata 990-8560, Japan

<sup>9</sup>Department of Earth and Space Science, Graduate School of Science, Osaka University, Toyonaka, Osaka 560-0043, Japan

<sup>10</sup>Department of Physical Science, Hiroshima University, 1-3-1 Kagamiyama, Higashi-Hiroshima, Hiroshima 739-8526, Japan

<sup>11</sup>Hiroshima Astrophysical Science Center, Hiroshima University, 1-3-1 Kagamiyama, Higashi-Hiroshima, Hiroshima 739-8526, Japan

<sup>12</sup>MAXI Team, RIKEN, 2-1 Hirosawa, Wako, Saitama 351-0198, Japan

\*E-mail: [takuya.akahori@nao.ac.jp](mailto:takuya.akahori@nao.ac.jp)

Received 2017 September 12; Accepted 2018 March 26

## Abstract

We report the Australia Telescope Compact Array 16 cm observation of CIZA J1358.9–4750. Recent X-ray studies imply that this galaxy cluster is composed of merging, binary clusters. Using the EW367 configuration, we found no significant diffuse radio emission in and around the cluster. An upper limit of the total radio power at 1.4 GHz is  $\sim 1.1 \times 10^{22} \text{ W Hz}^{-1}$  in 30 square arcminutes, which is a typical size for radio relics. It is known that an empirical relation holds between the total radio power and X-ray luminosity of the host cluster. The upper limit is about one order of magnitude lower than the power expected from the relation. Very young ( $\sim 70$  Myr) shocks with low Mach numbers ( $\sim 1.3$ ), which are often seen at an early stage of merger simulations, are suggested by the

previous X-ray observation. The shocks may generate cosmic-ray electrons with a steep energy spectrum, which is consistent with non-detection of bright ( $>10^{23} \text{ W Hz}^{-1}$ ) relic in this 16 cm band observation. Based on the assumption of energy equipartition, the upper limit gives a magnetic field strength of below  $0.68f(D_{\text{los}}/1 \text{ Mpc})^{-1}(\gamma_{\text{min}}/200)^{-1} \mu\text{G}$ , where  $f$  is the cosmic-ray total energy density over the cosmic-ray electron energy density,  $D_{\text{los}}$  is the depth of the shock wave along the sightline, and  $\gamma_{\text{min}}$  is the lower cutoff Lorentz factor of the cosmic-ray electron energy spectrum.

**Key words:** galaxies: clusters: individual (CIZA J1358.9–750)—intergalactic medium—magnetic fields—shock waves.

## 1 Introduction

In the large-scale structure formation, merging galaxy clusters release their huge gravitational energy into the thermal energy of the intracluster medium (ICM) (e.g., Sarazin 2002; Markevitch & Viklinin 2007). A merger sequence of two clusters can be divided into (i) the early stage, where the two clusters are getting close (e.g., Abell 399/401, Fujita et al. 2008), and (ii) the late stage, where they are receding from each other (e.g., Abell 3667, Nakazawa et al. 2009); an intermediate stage between these two phases occurs on a short time-scale because of high-speed crossing of the two gravitational potential cores. Hydrodynamic simulations suggest that shock waves with position-dependent Mach numbers,  $\mathcal{M}$ , arise in the merger (e.g., Ryu et al. 2003; Takizawa 2008; Akahori & Yoshikawa 2010). The shocks with  $\mathcal{M} < 2$  appear in the linking region of the two clusters in the early stage, while the shocks with larger Mach numbers,  $2 < \mathcal{M} < 4$ , appear ahead of the two receding cores in the late stage because the shocks propagate to cooler gas at cluster outskirts.

The merger stage is, therefore, one of the essential pieces of information in understanding the nature of cluster mergers. However, although shock waves and their Mach numbers are important clues for elucidating the merger stage, they are studied only in a limited number of bright X-ray clusters (e.g., Finoguenov et al. 2010; Akamatsu & Kawahara 2013; Itahana et al. 2015). Even though we know the presence of shocks, the merger stage is controversial in some clusters (e.g., RX J1347.5–1145, Kitayama et al. 2016). Significant effort has been ongoing over the last years to determine the merger stage by morphology of X-ray surface brightness, analysis of weak gravitational lensing, optical spectroscopy, and galaxy distribution (e.g., Okabe & Umetsu 2008; Okabe et al. 2011; Dawson 2013; Dawson et al. 2015; Okabe et al. 2015; Jee et al. 2016). For example, separation of a cD galaxy from the peak of X-ray surface brightness is frequently seen in the late stage of a merger (Abell 2163, Okabe et al. 2011).

Radio observation provides us with complementary information on the shock wave and the merger stage (e.g., Ozawa et al. 2015). Many clusters possess diffuse radio emissions, which are in general classified into radio halos, mini-halos, and relics, according to their size, location, morphology, and so on (see, e.g., Feretti et al. 2012 for a recent review). The connection between diffuse radio emission and the dynamical state of the system has been discussed (e.g., powerful radio halos in under-luminous X-ray clusters; Giovannini et al. 2011, and giant radio halos in cool core systems; Bonafede et al. 2014). Double-arc shapes seen in several radio relics suggest the presence of shock waves which appear in the late stage of mergers, although there are also radio relics that have more roundish shapes. The origin of such diversity amongst the relics has been intensively studied in the literature (see Feretti et al. 2012).

The cluster diffuse radio emission is likely synchrotron radiation, suggesting the presence of an intracluster magnetic field and cosmic-ray electrons (CRes). Because a GeV CRe emitting synchrotron radiation in the GHz band has a short lifetime, the emission would be associated with fresh CRes which are recently accelerated (e.g., Sarazin 1986; Enßlin et al. 1998; Carilli & Taylor 2002). For the merger shocks, diffusive shock acceleration (DSA) has been studied in the literature (e.g., Blandford & Eichler 1987; Kang & Ryu 2013; Vazza & Brüggén 2014). This theory can link the spectral index of radio emission with the shock Mach number. However, the standard DSA (the first-order Fermi acceleration) suffers from a low efficiency of acceleration, particularly at a shock with a low Mach number. To overcome this injection problem, other mechanisms have been studied, such as shock drift acceleration (SDA, e.g., Matsukiyo et al. 2011; Caprioli & Spitkovsky 2014; Guo et al. 2014; Matsukiyo & Matsumoto 2015) and second-order Fermi (re-)acceleration (Fujita et al. 2015, 2016; Kang et al. 2017). van Weeren et al. (2017) found a radio emission and interpreted it as synchrotron radiation from the CRes which were originally injected by an active

galactic nucleus (AGN) and were recently re-accelerated by a cluster merger shock.

Various mechanisms take place in the structure formation; shock heating, eddy cascading (turbulence), cosmic-ray acceleration, and magnetic-field amplification, as well as radiative cooling, AGN feedback, and metal enrichment. Therefore, observational diagnostics of energy budgets in galaxy clusters is crucially important in understanding the structure formation history. Thermal and non-thermal energies in the ICM can be partly estimated from X-ray continuum emission and synchrotron emission, respectively. It is known that a correlation holds between the radio power,  $P$ , and the X-ray luminosity,  $L_X$ , of the host cluster. This  $L_X$ - $P$  relation applies to both radio halos and relics (e.g., Brunetti et al. 2007, 2009; Rudnick & Lemmerman 2009; Cassano et al. 2010, 2013; Enßlin et al. 2011; Feretti et al. 2012; Xu et al. 2012; Govoni et al. 2013; de Gasperin et al. 2014; Kale et al. 2015) and even to radio mini-halos in cool-core clusters (Gitti et al. 2015).

Although many late-stage clusters have been observed, there are only a small number of candidates of early-stage clusters, and little is known about shock waves, radio emission, the radio spectral index, and the  $L_X$ - $P$  relation in the early stage (e.g., Akamatsu et al. 2016). In the present paper, we report the first 16 cm (1–3 GHz) observations of CIZA J1358.9–4750 (hereafter CZ1359), which is a candidate early-stage cluster. We discuss the nature of CZ1359, such as its merger scenario and particle acceleration. This paper is organized as follows. We describe the observations and data reduction in sections 2 and 3, respectively. Results are shown in section 4. Our discussion is presented in section 5, followed by concluding remarks in section 6.

## 2 Radio observations

### 2.1 The target

CZ1359 is a nearby (redshift  $z \sim 0.07$ ) galaxy cluster listed in the X-ray cluster catalog, CIZA (the Clusters in the Zone of Avoidance, Ebeling et al. 2002; Kocevski et al. 2007). This object exhibits two X-ray surface brightness enhancements in the southeast and northwest directions with a separation of  $14' \sim 1.2$  Mpc. The enhancements are likely sub-clusters and the separation is  $\sim 0.7$ – $0.8$  times smaller than the virial radius ( $r_{200}$ , Kato et al. 2015) of each sub-cluster. Each X-ray core possesses a giant elliptical galaxy, which does not significantly deviate from the X-ray center.

Kato et al. (2015) observed CZ1359 with the Suzaku X-ray telescope, and found that the ICM in the linking region between the cores is  $\sim 30\%$  hotter than the ICM around the cores. Moreover, they discovered a temperature jump in the region and confirmed an associated

X-ray brightness jump in an archival XMM-Newton image. Applying the Rankine–Hugoniot condition to the largest temperature increase, they estimated the Mach number of the shock,  $\mathcal{M} = 1.32 \pm 0.22$ . This number is broadly consistent with a prediction by numerical simulations ( $\mathcal{M} \sim 1.5$ , Akahori & Yoshikawa 2008, 2010).

The coincidental position of giant elliptical galaxies with X-ray cores, the X-ray brightness enhancement, and the X-ray temperature jumps all suggest that CZ1359 is in the early stage of merger, though further evidence such as radio emission is helpful to understand its thermal and dynamical state. There are no scientific centimeter observations covering the CZ1359 field, except the 843 MHz Sydney University Molonglo Sky Survey (SUMSS) shallow survey (Bock et al. 1999). There are also two 150 MHz surveys that are publicly available: the TIFR GMRT Sky Survey (TGSS) (Intema et al. 2017) and the GaLactic and Extragalactic All-sky MWA survey (GLEAM) (Hurley-Walker et al. 2017). All of these surveys detected several compact sources in the CZ1359 field (section 4), but no diffuse radio emission (L. T. George & R. Kale 2015 private communication).

### 2.2 The observation

In order to explore possible radio halos, mini-halos, and relics in the CZ1359 field, we carried out a deep centimeter observation of the entire CZ1359 field which extends to  $\sim 30'$  in diameter. The observation was made with the Australia Telescope Compact Array (ATCA). We adopted the 16 cm band (from 1.1 GHz to 3.1 GHz) which gives a field-of-view of  $22.3$  at the center frequency, 2.1 GHz. The observation required a trade-off between (i) an array configuration as compact as possible to gain a better sensitivity for diffuse emission, and (ii) a beam size of  $\sim 1'$  or better so as to identify arc-shaped structures of potential relics. We adopted the EW367 array configuration in which all six antennas were mounted in the east–west track. The minimum baseline was 46 m and the largest well-imaged structure at 2.1 GHz is  $\sim 20'$ .<sup>1</sup> The maximum baseline was 367 m without the distant antenna 6 (CA06), and 4408 m with CA06. Resultant beam position angles and beam major/minor axes at 2.1 GHz were  $-89^\circ$  and  $\sim 23'' \times 20''$  with CA06, and  $-1.6^\circ$  and  $\sim 137'' \times 91''$  without CA06, respectively.

We adopted four pointings to cover the CZ1359 field. About a half of each primary beam overlaps the other beams. The observations were performed on 2014 June 6

<sup>1</sup> The largest well-imaged structure of 1-d observation is  $\sim 230''$  at 6 cm with the 750 m configuration (sub-subsection 1.7.1 of ATCA Users Guide ([http://www.narrabri.atnf.csiro.au/observing/users\\_guide/html/atug.html](http://www.narrabri.atnf.csiro.au/observing/users_guide/html/atug.html))). It scales  $230'' \times 2 \times 16/6 \sim 20'$  at 16 cm with the 367 m configuration.

**Table 1.** Observation log of CZ1359 with the ATCA.

Pointing	Right ascension (J2000.0)	Declination (J2000.0)	Date	Period (UT)	Frequency (MHz)	Bandwidth (MHz)	Exposure (min)
NE	13:59:10.0	-47:41:00.0	2014 June 06	04:58–16:37	1100–3100	2048	560
NW	13:58:10.0	-47:40:00.0	2014 June 08	05:02–17:06	1100–3100	2048	595
SE	13:59:10.0	-47:52:00.0	2014 June 09	04:30–16:36	1100–3100	2048	595
SW	13:58:00.0	-47:51:00.0	2014 June 10	04:31–16:46	1100–3100	2048	560

(northeast, NE), June 8 (northwest, NW), June 9 (southeast, SE), and June 10 (southwest, SW) (PI: T. Akahori, ID: C2916). The parameters of these pointings are listed in table 1. Observation time for each pointing was 12 hours in total, including the overhead of standard calibration and antenna slew time. On-target exposure times were 9.33, 9.92, 9.92, and 9.33 hr in total for NE, NW, SE, and SW, respectively. Such a long tracking provided us with good hour angle coverage.<sup>2</sup> The system temperature was between 38 K (meridian passage) and 50 K (rising and setting) and those were stable during the observing days.

On each day, we observed the calibrator 0823–500 for 10 minutes at the start of the schedule, the band-pass calibrator 1934–638 (12.6 Jy at 2.1 GHz, a compact source, no linear polarization, where  $1 \text{ Jy} = 10^{-26} \text{ W Hz}^{-1} \text{ m}^{-2}$ ) for 10 minutes in the middle and at the close of the schedule, and the gain/phase calibrator 1421–490 (7.38 Jy at 2.1 GHz; the distance from the target is  $4.48^\circ$ ) for three minutes of every 35 minutes of on-target observations. The 1M-0.5k Compact Array Broadband Backend (CABB, Wilson et al. 2011) receiver mode was selected to allow full spectro-polarimetry observations. The raw spectral channel is 1 MHz and the bandwidth is 2048 MHz.

### 3 Data reduction

We performed the standard ATCA data reduction using the MIRIAD software (version 1.5) as follows. All data were loaded by the MIRIAD task ATLOD with options BIRBIE, RFIFLAG, XYCORR, and NOAUTO. 40 channels at the band edges that are likely affected by the bandpass rolloff were removed by UVFLAG. Data were then split into subsets for the band-pass calibrator, the gain/phase calibrator, and the target, using UVSPLIT. For each subset, we performed UVFLAG, PGFLAG, and BLFLAG to flag out radio frequency interferences (RFIs). These were done iteratively until RFI signals disappeared from the visibility plots. The band-pass solution was made by MFCAL, using the subset of the band-pass calibrator. The solution was transferred to the

gain/phase calibration by GPCOPY, and then GPCAL was carried out to obtain the gain and phase solutions. The error of the absolute value was computed by bootstrap estimation using GPBOOT. Finally, all solutions were applied to the target data using GPCOPY and GPAVER.

The visibility data were transformed into images using INVERT, where the robustness parameters,  $r = 0.5$  and  $2.0$ , were chosen to optimize the images for the studies of compact and diffuse sources, respectively. We created the images including CA06, which gives the longest baselines and improves the angular resolution. We also created the images excluding CA06, because it makes the image rms noise level worse due to the large side-lobes caused by large uv gaps between the longest baselines and the others. The deconvolution was carried out using MFCLEAN, where we employed the best iteration number which minimized the rms noise on the cleaned image. Finally, four pointing images were linearly combined into a mosaic image using LINMOS.

The Stokes  $I$  images were successfully reduced and the flux scale was verified using a SUMSS source (appendix 1). The 128, 512, and 2048 MHz bandwidth images were made to compare the rms noise levels. Here, in the 128 MHz case, we did not consider the bottom (1140 MHz) and top (3060 MHz) bands, since the noise levels were high due to RFIs. Figure 1 summarizes the rms noise levels we have achieved with the robustness  $r = 2.0$ . Typical noise levels were  $0.5 \text{ mJy beam}^{-1}$  (1.5–2 GHz) and  $0.3 \text{ mJy beam}^{-1}$  (2–3 GHz). Meanwhile, Stokes  $Q$  and  $U$  images have no significant signal. We did not obtain reliable noise levels of Stokes  $Q$  and  $U$  because of artefacts in the images.

The typical noise levels were several times worse than the theoretical rms noise level (e.g.,  $0.038 \text{ mJy beam}^{-1}$  at 2036 MHz with a 128 MHz bandwidth). This is thought to be mostly due to a very bright source, PMN J1401–4733 (or SUMSS J140158–473336), located at the edge of each pointing image. The total intensity of this source,  $0.433 \text{ Jy beam}^{-1}$  at 1524 MHz, was  $\sim 1000$  times higher than the image rms noise level, and this strong signal inevitably produces frequency-dependent sidelobes. Actually, the sidelobe effect caused the noise to be highest in the NE images, and increasing the bandwidth above 128 MHz did not improve the image rms noise level, as shown in

<sup>2</sup> The ATCA uses dual linear orthogonal feeds to measure two orthogonal linear polarizations simultaneously. The position angle of the polarization splitter is stationary with respect to the ultra-azimuthal-mounted antennas and so rotates on the sky.

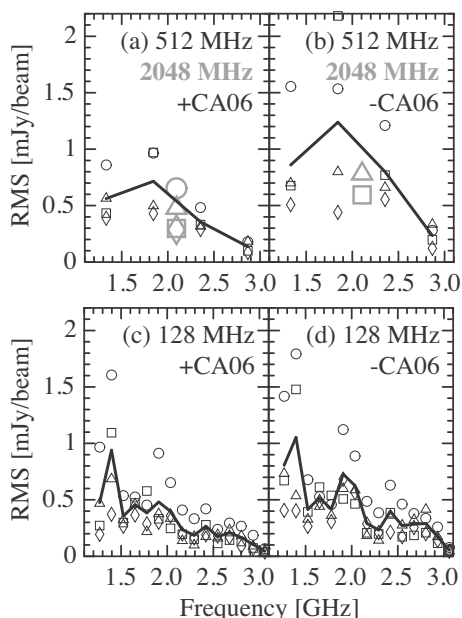


**Fig. 1.** (a) Image rms noise levels for the NE (circles), NW (boxes), SE (triangles), and SW (diamonds) pointings with 512 MHz (black) and 2048 MHz (gray) bandwidth. The solid line is the average for the four pointings of 512 MHz bandwidth. (b) The same as (a) but without CA06 baselines. Note that rms noise levels of NE ( $51.26 \text{ mJy beam}^{-1}$ ) and SW ( $4.730 \text{ mJy beam}^{-1}$ ) for a 2048 MHz bandwidth are outside the frame of (b). (c), (d) Same as (a) and (b), respectively, but with a 128 MHz bandwidth.

figure 1. The sidelobe effect cannot be removed by tuning the robustness and taper parameters in imaging, nor by iterating the CLEAN algorithm. We also performed self-calibration, but the noise level remains within  $\pm 10\%$ – $20\%$ , depending on the direction (NE, NW, SE, SW) and the frequency. Therefore, hereafter we only show our results without taking self-calibration.

## 4 Result

We first report compact sources found in the CZ1359 field, and then explore diffuse sources. As mentioned, visibility data were imaged with the robustness  $r = 0.5$  for compact sources and  $r = 2.0$  for diffuse sources to optimize each detection.

### 4.1 Compact sources

Radio compact sources which have fluxes larger than the detection limit ( $>5\sigma$ ) were explored, and 12 reliable compact sources were found. Here, by eye, we rejected several spurious sources (not listed) which were unreliable in the two senses that (i) they only appear in less than half of the 128 MHz band images, or (ii) their positions depend on frequency and move beyond angular resolutions. The locations of the detected compact sources are shown in figure 2

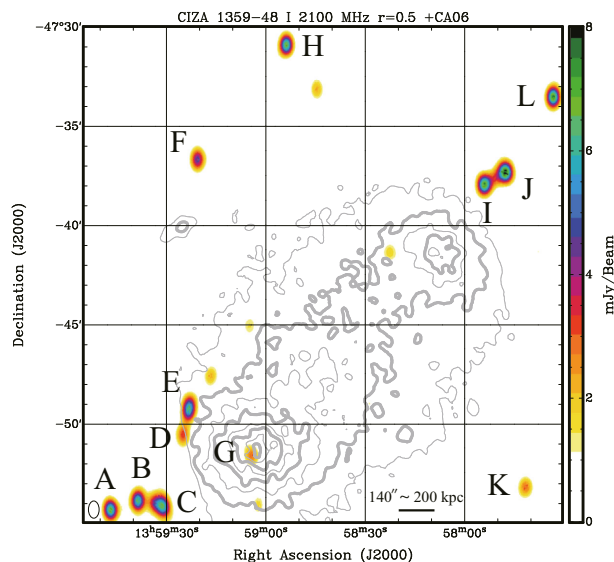


**Fig. 2.** Total intensity map of CZ1359 at 2100 MHz with a 2048 MHz bandwidth and with CA06 baselines. Gray contours show the X-ray surface brightness (Kato et al. 2015). (Color online)

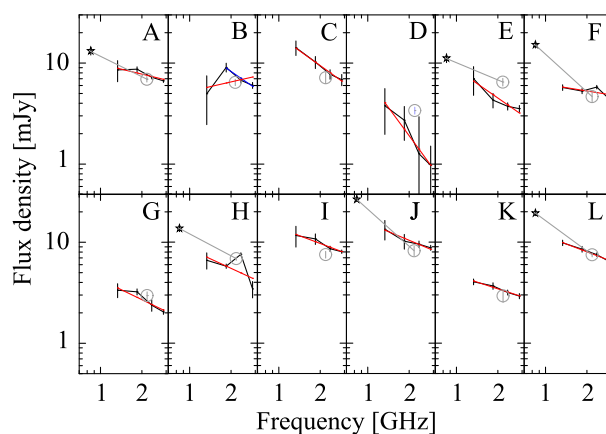


**Fig. 3.** Radio intensity spectra for 12 compact sources in the CZ1359 field. Solid lines and gray circles show the ATCA 512 MHz and 2048 MHz bandwidth data, respectively. Stars indicate the data of SUMSS. Red lines are best fits of the ATCA 512 MHz data only. The blue line for Source B is the best fit without the bottom band data (see the text). Gray lines are best fits of the SUMSS + ATCA 2048 MHz bandwidth data. (Color online)

with alphabetic labels from east to west. The spectra of these sources are shown in figure 3.

Table 2 summarizes the source coordinate and source peak flux, which were derived using the MIRIAD task IMFIT with an option OBJECT=POINT. Also listed is the spectral index,  $\alpha_{\text{obs}}$ , which was obtained from a least-squares fit of our 512 MHz bandwidth spectra with the simple power-law form

$$I_\nu \propto \nu^{-\alpha_{\text{obs}}}, \quad (1)$$

**Table 2.** Summary of compact sources in the CZ1359 field.

ID	Right ascension (error in arcsec)	Declination (error in arcsec)	This work* (mJy beam <sup>-1</sup> )	$\alpha_{\text{obs}}$	TGSS <sup>†</sup> (mJy beam <sup>-1</sup> )	SUMSS <sup>‡</sup> (mJy beam <sup>-1</sup> )	2MASX	$\alpha_{\text{obs}}^{\text{SUMSS+ATCA}}$
A	13:59:46.536 (1.139)	-47:54:14.37 (0.975)	6.96 ± 0.44	0.33	18.32	13.2 ± 1.2	—	0.67
B	13:59:37.828 (1.342)	-47:53:52.25 (1.142)	6.45 ± 0.47	0.94	16.16	—	—	—
C	13:59:31.085 (1.455)	-47:54:06.73 (1.239)	7.16 ± 0.92	0.98	21.76	—	Yes	—
D	13:59:24.841 (1.613)	-47:50:19.07 (1.431)	3.39 ± 0.26	1.86	—	—	Yes	—
E	13:59:22.770 (1.625)	-47:49:05.25 (1.411)	6.53 ± 0.57	0.95	—	11.2 ± 1.1	Yes	0.57
F	13:59:19.316 (1.559)	-47:36:41.85 (1.344)	4.68 ± 0.51	0.22	34.83	15.2 ± 1.1	—	1.24
G	13:59:03.488 (1.987)	-47:51:33.62 (1.709)	2.99 ± 0.26	0.66	—	—	Yes <sup>§</sup>	—
H	13:58:53.790 (1.151)	-47:30:55.74 (0.985)	6.89 ± 0.26	0.63	17.39	13.7 ± 1	—	0.72
I	13:57:53.588 (1.382)	-47:37:48.99 (1.186)	7.49 ± 0.57	0.51	45.39	—	Yes	—
J	13:57:47.991 (1.508)	-47:37:19.39 (1.290)	8.28 ± 0.89	0.57	44.29	26.4 ± 1.3	—	1.22
K	13:57:41.723 (0.975)	-47:53:03.78 (0.827)	2.94 ± 0.41	0.44	16.04	—	—	—
L	13:57:33.947 (1.271)	-47:33:33.36 (1.086)	7.49 ± 0.34	0.52	64.88	19.4 ± 1.1	—	1.00

\*Flux at 2100 MHz.

†Flux at 150 MHz.

‡Flux at 843 MHz.

§See also the text.

where  $\nu$  is the frequency. Only Source B indicates a positive slope (a negative spectral index) with  $\alpha_{\text{obs}} = -0.31$ , though the fit is affected by the bottom-band data which have large errors. Without the bottom band, we obtain  $\alpha_{\text{obs}} = 0.94$  (the blue line in figure 3), which is adopted in table 2.

We checked TGSS images and the SUMSS catalog to look for possible counterpart emission, where the search range was set to be 30'' (about one and a half beam size) in radius. We also searched for possible association of extragalactic objects using the NASA Extragalactic Database (NED). The results found in TGSS (150 MHz) images, the SUMSS (843 MHz) catalog, and the 2MASX (near-infrared) database are listed in table 2. The spectral index,  $\alpha_{\text{obs}}^{\text{SUMSS+ATCA}}$ , was derived using the SUMSS data and our 2048 MHz bandwidth data.

It is found that Source G, which has no TGSS or SUMSS counterparts, is located near the center of the SW cluster 2XMM J135904.3–475125 (13:59:04.3, -47:51:25). A superposed map at 2292 MHz is shown in figure 4, where the coordinate errors of right ascension and declination are 1'42 and 1'23, respectively, and the beam major/minor axes are 19''.79 × 17''.23. The peak position of the radio emission deviates from that of the X-ray by about one beam size (~20'' or ~30 kpc at  $z = 0.07$ ). It also deviates from the central galaxy 2MASX J13590381–4751311 (13:59:03.8, -47:51:31), and a nearby galaxy 2MASX J13590223–4751502 (13:59:02.2, -47:51:50) each by about half a beam size. The size of Source G is at least smaller than ~40 kpc and the spectral index is 0.66. These features could be explained by AGN emission in the cluster or background, the host galaxy of which is one of the two 2MASX sources or is too faint to list in the 2MASX catalog.

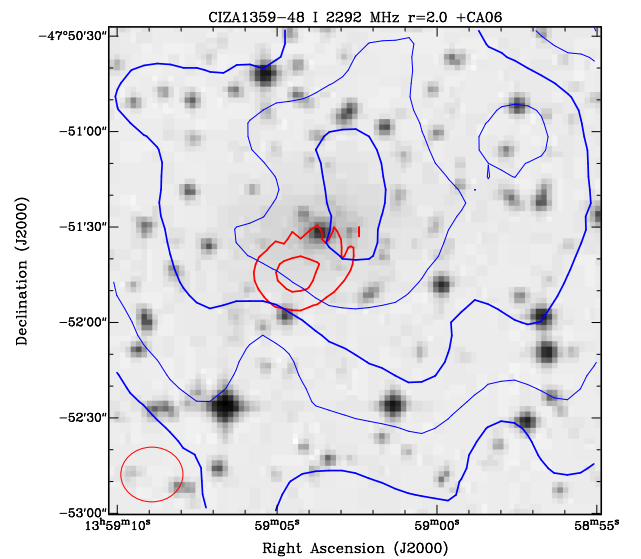


**Fig. 4.** Superposed image near the center of southeast sub-cluster of CZ1359. Background is the DSS optical image. Blue contours are the Suzaku X-ray surface brightness. Red contours are 2.3 GHz radio continuum images for a 128 MHz bandwidth with levels of 1 mJy beam<sup>-1</sup> (5.4 $\sigma$ ) and 2 mJy beam<sup>-1</sup> (10.7 $\sigma$ ). Also shown at the bottom left is the beam size of the radio image. (Color online)

With the spectral index of 0.66, the expected flux densities at 150 MHz and 843 MHz are 17.1 mJy and 5.46 mJy, both of which are below the detection limits of TGSS and SUMSS, respectively.

## 4.2 Diffuse sources

Figure 5a shows the CA06-included Stokes  $I$  image at 2036 MHz with a 128 MHz bandwidth, where gray contours represent the X-ray surface brightness

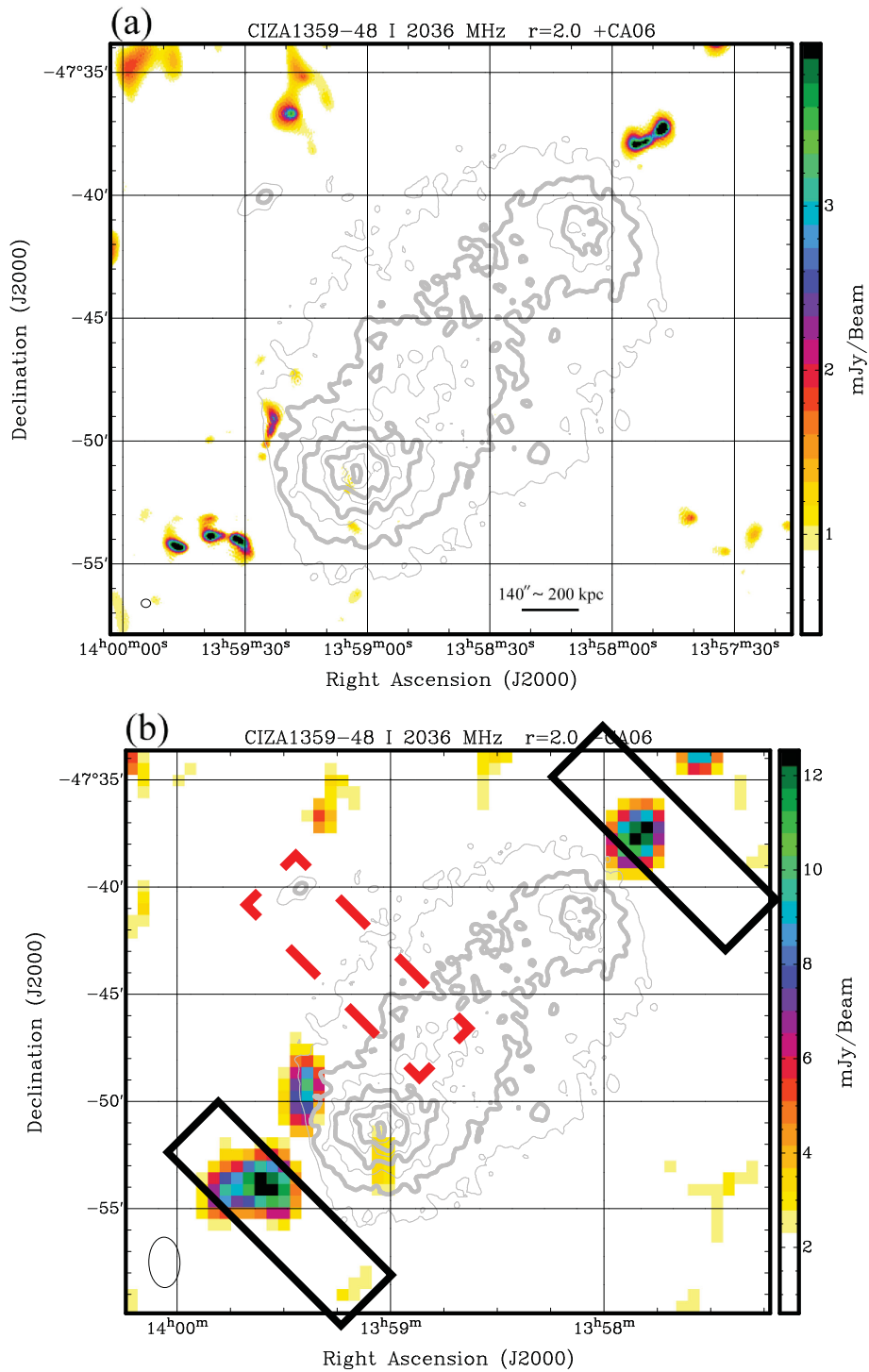


**Fig. 5.** Total intensity map of CZ1359 at 2036 MHz with a 128 MHz bandwidth (a) with CA06 baselines and (b) without CA06 baselines. The color range is shown from  $1\sigma$  to  $10\sigma$  rms noise level. Gray contours show the X-ray surface brightness (Kato et al. 2015). The black solid and red dashed boxes indicate  $10' \times 3'$  areas in which radio relics are expected in the late- and early-stage of cluster merger, respectively; the latter is associated with the observed X-ray shock front (Kato et al. 2015; subsection 5.4). (Color online)

(Kato et al. 2015) for reference. We only found compact sources, and did not detect diffuse sources in the CZ1359 field. The CA06-excluded image is also shown in figure 5b. There are apparently extended emissions, but all of them

are consistent with compact sources convolved with a low-resolution beam, or noise. Because the largest well-imaged structure ( $\sim 20'$ ) should be enough to detect possible diffuse emission in the CZ1359 field, it is unlikely that we miss the

diffuse emission due to a lack of short baselines of the interferometry. We have checked all 128, 512, and 2048 MHz bandwidth images, and found no diffuse emission among any of them.

Let us consider a typical, bright diffuse emission, i.e. radio halo and relic, possessing a surface brightness of  $1 \mu\text{Jy arcsec}^{-2}$  at 1.4 GHz with  $\alpha_{\text{obs}} \sim 1$  (Feretti et al. 2012). For the SUMSS at 843 MHz with a beam size of  $2295 \text{ arcsec}^2$ , the brightness becomes  $3.8 \text{ mJy beam}^{-1}$  or only  $\sim 3$  times its sensitivity limit. Meanwhile, for our observation at 2.1 GHz with beam size  $14126 \text{ arcsec}^2$  (without CA06), the brightness becomes  $9.5 \text{ mJy beam}^{-1}$  or  $\sim 20$ – $30$  times the achieved sensitivity limit. Therefore, our non-detection firmly excludes the presence of bright diffuse emission in the CZ1359 field. Even a faint case of  $0.1 \mu\text{Jy arcsec}^{-2}$  is excluded at a  $\sim 3\sigma$  level.

We derive the upper limit of radio power ( $\text{W Hz}^{-1}$ ) from the integration of the intensity,

$$P = 4\pi D_L^2 \int I d\Omega \sim 4\pi D_L^2 I_{\text{rms}} A_{\text{beam}} \sqrt{A_{\text{lim}}/A_{\text{beam}}}, \quad (2)$$

where  $D_L$  is the luminosity distance in meters,  $I_{\text{rms}}$  the noise level in  $\text{Jy arcsec}^{-2}$ ,  $A_{\text{beam}}$  is the beam area in  $\text{arcsec}^2$ , and  $A_{\text{lim}}$  is the upper-limit area in  $\text{arcsec}^2$ . Because the upper-limit area considered below is larger than the beam area, the flux upper-limit is given according to the error propagation; the error on a flux measurement scales with the square root of the ratio of the upper-limit area and beam area.

We adopt  $D_L(z = 0.07) \sim 9.74 \times 10^{24} \text{ m}$  for the cosmological parameters  $H_0 = 70 \text{ km s}^{-1} \text{ Mpc}^{-1}$ ,  $\Omega_M = 0.3$ , and  $\Omega_\Lambda = 0.7$ . The noise level is  $I_{\text{rms}} = 0.5 \text{ mJy beam}^{-1}$  at 1.4 GHz, where the beam size ( $A_{\text{beam}}$ ) at 1396 MHz is  $955.9 \text{ arcsec}^2$  with CA06 and  $29741 \text{ arcsec}^2$  without CA06. The upper-limit area is determined such that radio relics typically extend over a size several times larger than the cores of merging galaxy clusters (Feretti et al. 2012). If we consider a relatively large (i.e., conservative) upper-limit area of  $30 \text{ arcmin}^2$  shown in figure 5, we obtain the upper limit of radio power at 1.4 GHz to be  $P_{1.4} = 6.34 \times 10^{22} \text{ W Hz}^{-1}$  with CA06 and  $P_{1.4} = 1.14 \times 10^{22} \text{ W Hz}^{-1}$  without CA06. If we consider a typical, large radio halo with an area of  $1 \text{ Mpc}^2$  (Feretti et al. 2012) or  $144 \text{ arcmin}^2$  in the CZ1359 field, we obtain  $P_{1.4} = 1.39 \times 10^{23} \text{ W Hz}^{-1}$  with CA06 and  $2.49 \times 10^{22} \text{ W Hz}^{-1}$  without CA06.

Figure 6 shows the  $L_X$ – $P_{1.4}$  relation taken from Feretti et al. (2012). The arrow depicts the upper limit of CZ1359,  $P_{1.4} = 1.14 \times 10^{22} \text{ W Hz}^{-1}$ , against the X-ray luminosity,  $L_X = 3.14 \times 10^{44} \text{ erg s}^{-1}$ , derived from the Suzaku X-ray observation (Kato et al. 2015). Here, so as to compare with the other ROSAT data in Feretti et al. (2012), we derived

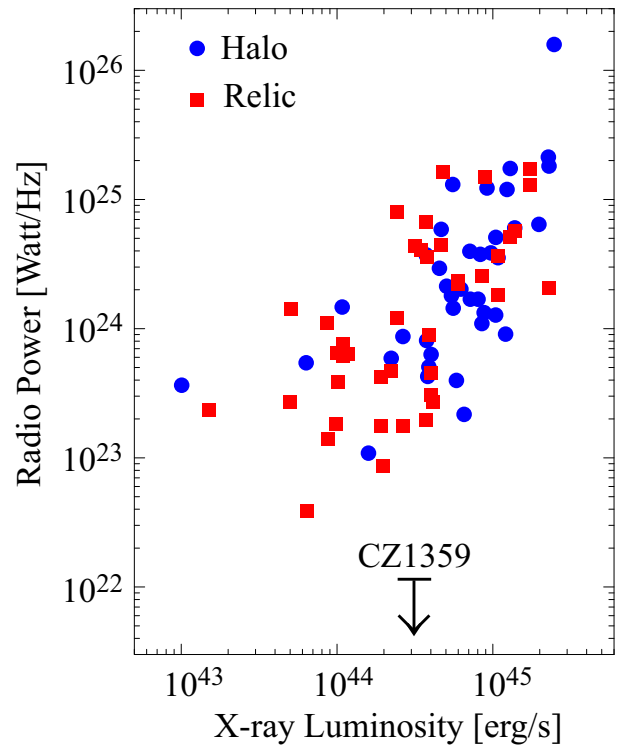


Fig. 6. Correlation between the radio power at 1.4 GHz and the 0.1–2.4 keV X-ray luminosity of 39 radio relics (red squares) and 41 radio halos (blue circles), all taken from Feretti et al. (2012). The black arrow indicates the upper limit of this work for a radio relic derived in section 4. (Color online)

the 0.1–2.4 keV luminosity from the bolometric luminosity, temperature, and metal abundance. We summed up the X-ray luminosities of the two sub-clusters as the total X-ray luminosity of the system, following studies of other clusters.

The upper limit of CZ1359 falls by one to two orders of magnitude lower than the  $L_X$ – $P_{1.4}$  relation. This observation first determined a strong upper limit of radio emission for a known intracluster shock with  $\mathcal{M} \sim 1.3$ . To date, there are several observations which introduce similar upper limits of Mpc-scale radio emission with the radio power of  $\lesssim 10^{23} \text{ W Hz}^{-1}$  around the X-ray luminosity of  $\sim 10^{44}$ – $10^{45} \text{ erg s}^{-1}$  (not shown, as it makes the plot crowded; see, e.g., Kale et al. 2015). The upper limit of CZ1359 is a factor of several lower than the limits obtained in previous works.

## 5 Discussion

The non-detection of diffuse radio emission in the CZ1359 field may be ascribed to various reasons. One of the potential explanations would be the collision impact parameter and viewing angle, both of which can alter apparent morphology (e.g., Akahori & Yoshikawa 2010). While this

geometrical dilution of radio halos and mini-halos is not well-known, relics can be significantly diluted if the shock surface is nearly perpendicular to the line-of-sight (LOS). However, Kato et al. (2015) discussed bulk velocities of member galaxies and concluded that the collision takes place almost parallel to the sky plane. Therefore, the geometrical effect could be minor.

At the X-ray shock front, the expansion speed of the post-shock region is estimated to be  $2400 \text{ km s}^{-1}$  (Kato et al. 2015). Since the apparent thickness of the shock-heated region is  $120''$  (168 kpc), the shock age is expected to be 68 Myr. This timescale is at least one order of magnitude shorter than the GeV electron cooling time (Sarazin 1999). Therefore, the underluminous radio emission cannot be caused by synchrotron cooling.

A more realistic explanation would be that CRe are not accelerated and/or magnetic fields are not amplified enough, and hence synchrotron emission is too weak to be observed. In order to argue the possibilities, we discuss CRe content and magnetic-field strength below. For this purpose, we consider potential radio relic regions each with a size of  $10' \times 3'$ , as shown in figure 5b. The red dashed box indicates the X-ray shock region (Kato et al. 2015), and the black solid boxes corresponds to potential late-stage shock regions.

Supposing a simple power-law of the CRe energy spectrum and the standard formula of synchrotron radiation (appendix 2), we have the following relation between the index of integrated (observed) radio spectra,  $\alpha_{\text{obs}}$ , the index of injected radio spectra,  $\alpha_{\text{inj}}$ , the shock Mach number,  $\mathcal{M}$  ( $>1$ ), and the CRe energy spectral index,  $p$ :

$$\alpha_{\text{obs}} = \alpha_{\text{inj}} + \frac{1}{2} = \frac{\mathcal{M}^2 + 1}{\mathcal{M}^2 - 1} = \frac{p}{2}, \quad (3)$$

(e.g., Blandford & Eichler 1987; Trasatti et al. 2015). Figure 7 shows the  $P_{1.4}$ - $\alpha_{\text{obs}}$  relation taken from Feretti et al. (2012). The vertical line indicates the upper limit of our observation,  $P_{1.4} = 1.14 \times 10^{22} \text{ W Hz}^{-1}$ . The arrow depicts  $\alpha_{\text{obs}} \sim 3.9$  derived from  $\mathcal{M} \sim 1.3$  of the X-ray shock, and this gives a very steep slope,  $p = 7.8$ . Meanwhile, many observed relics have  $\alpha_{\text{obs}} \sim 1.0$ – $1.5$ . This corresponds to  $\mathcal{M} \sim 2$ – $4$  in the DSA picture. Such a range of the Mach number is supported by numerical simulations and is common for the late-stage shock.

Under the assumption of the minimum energy equipartition (appendix 2), the steep spectrum of  $p = 7.8$  for the X-ray shock gives a very small CRe density and negligible intensity  $I \sim 1.06 \times 10^{-8} f^{-1} \text{ mJy beam}^{-1}$ , where  $f$  is the ratio of the cosmic-ray energy density over the cosmic-ray electron energy density. Therefore, the non-detection of diffuse

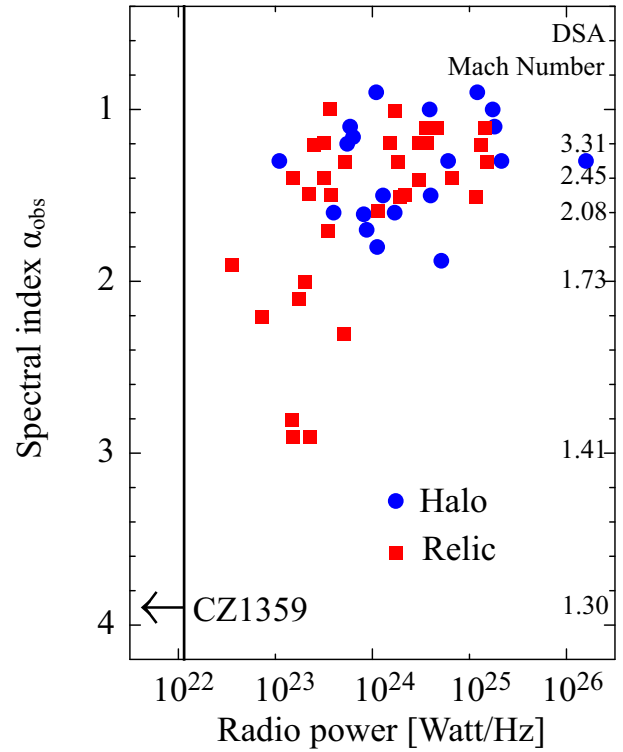


Fig. 7. Correlation between the radio power at 1.4 GHz and the spectral index  $\alpha_{\text{obs}}$ , all taken from Feretti et al. (2012). The black arrow indicates the constraint on CZ1359 from the present work (see text for details). (Color online)

radio emission at the X-ray shock front can be explained by the standard DSA scenario.

As a cross-check, let us consider a case in which CZ1359 hosts a  $\alpha \sim 1.5$  relic or halo, but is just dim. Our upper limit of  $0.5 \text{ mJy beam}^{-1}$  at 1.4 GHz and representative values  $(p, \gamma_{\text{min}}, \gamma_{\text{max}}, D_{\text{los}}) = (3, 200, 3000, 1 \text{ Mpc})$  gives  $B < 0.682f \mu\text{G}$ , where  $D_{\text{los}}$  is the depth of the shock along the LOS.  $\gamma_{\text{min}}$  and  $\gamma_{\text{max}}$  are the minimum and maximum Lorentz factor of the cosmic-ray electrons, respectively. The upper limit is approximately proportional to  $\gamma_{\text{min}}^{-1}$  for  $50 \leq \gamma_{\text{min}} \leq 600$ , and changes by only a few percent for  $\gamma_{\text{max}} > 3000$ . The upper limit excludes the presence of strongly-magnetized shocks with  $\mathcal{M} \gtrsim 2$  in the standard DSA scenario. The upper limit also gives the limit of the cosmic-ray electron density,  $n_{\text{ce}} < 6.03 \times 10^{-11} f \text{ cm}^{-3}$ . With the mean thermal electron density at a potential late-stage shock,  $n_e \sim 0.5 \times 10^{-3} \text{ cm}^{-3}$  (Kato et al. 2015), the injected fraction of CR electrons is  $\xi_e = n_{\text{ce}}/n_e < 1.21f \times 10^{-7}$ . This value is small compared to the efficiency estimated for a  $\mathcal{M} \sim 2$ – $4$  shock,  $\xi_e \sim 10^{-3}$ – $10^{-6}$  (see, e.g., Kang & Ryu 2013; Vazza & Brügggen 2014). Finally, the upper limit gives rather loose upper limits of the non-thermal to thermal energy budget,  $\varepsilon_{\text{NT}}/\varepsilon_{\text{T}} < 4.0f^2\%$  and  $< 3.1f^2\%$  for the temperature  $T_e = 4.6 \times 10^7 \text{ K}$  (north) and  $T_e = 5.8 \times 10^7 \text{ K}$  (south), respectively (Kato et al. 2015).

Note that we have used the Mach number measured from the X-ray observation. However, an inconsistency among the Mach numbers derived from X-ray and radio observations has been reported in the literature (e.g., Akamatsu & Kawahara 2013; Ogrea et al. 2013; Itahana et al. 2015). Therefore, there might exist a discrepancy between a radio-derived spectral index and an X-ray-derived spectral index.

Finally, let us consider the picture beyond the DSA. A simple DSA model assumes that cosmic rays are well-accelerated with sufficient acceleration time. This may not be the case for the X-ray shock with an age of 68 Myr (Kato et al. 2015), in that both field amplification and particle acceleration may be in progress, resulting in the synchrotron emission being too weak to be detected. This scenario implies a weak pre-amplified magnetic field and fewer seed cosmic-ray electrons in the linking region of the cluster. Nevertheless, low-energy cosmic-ray electrons, which emit radio synchrotron at low frequencies and not in the GHz band, may exist on some level. Thus, low-frequency deep observations will be an important next step.

Recently, Fujita et al. (2015) and Fujita, Akamatsu, and Kimura (2016) proposed that cluster diffuse radio emission can be produced through the second-order Fermi (re-)acceleration, which is different from the DSA (the first-order Fermi acceleration, see also Kang et al. 2017). Even if the second-order Fermi acceleration is taking place, electrons may not have had enough time to be accelerated, or scatterers of electrons (e.g., turbulence) may not have developed well behind the shock. Numerical simulations suggest that the early-stage merging clusters have relatively weak turbulence, which is also consistent with non-detection of radio halo in CZ1359.

## 6 Conclusion

We conducted an ATCA 16 cm observation of a merging galaxy cluster, CIZA J1358.9–4750 (CZ1359). In the CZ1359 field, we first obtained a significant upper limit of diffuse emission, which was about one order of magnitude lower than was estimated using the X-ray luminosity–radio power relation for bright radio halos and relics. Therefore, an environment of this merging-cluster system is different from the clusters possessing typical, bright radio halos and relics. Using the upper limit of total intensity and assuming a model of shock acceleration, we first derived non-thermal properties at the X-ray shock front and potential shock fronts in CZ1359.

Because a steep spectral index is expected due to a low ( $\sim 1.3$ ) Mach number, low-frequency deep

observations with Murchison Widefield Array (MWA) and Giant Metrewave Radio Telescope (GMRT) are important to investigate possible diffuse radio emission in the CZ1359 field further. In future, the Square Kilometre Array (SKA) and its precursors, Australian SKA Pathfinder (ASKAP) and MeerKAT, will provide an unprecedented sensitivity in the Southern hemisphere (Johnston-Hollitt et al. 2015). They will advance the study of this cluster significantly.

## Acknowledgments

The authors acknowledge Mr. Lijo Thomas George and Dr. Ruta Kale for their kind attention and checking of TGSS and GLEAM data. The authors would also like to thank the anonymous referee for his/her constructive comments and suggestions. This work was supported in part by JSPS KAKENHI Grant Numbers 26400218(MT), 15H03639(NK, TA), 15K05080(YF), 15K17614(TA), and by an University Research Support Grant from the National Astronomical Observatory of Japan (NAOJ). The Australia Telescope Compact Array is funded by the Commonwealth of Australia for operation as a National Facility managed by CSIRO.

## Appendix 1 Flux scale

Since there is no previous 16 cm observation of the CZ1359 field, we tried to verify our flux scale by comparing our result with the survey data of TGSS (150 MHz) and SUMSS (843 MHz). The comparison was performed for a bright compact source SUMSS J140033–473800 (14:00:33.5, –47:38:00) in the CZ1359 field. We carried out the linear fit for the spectrum using data at 1844, 2356, and 2868 MHz with each 512 MHz bandwidth. Here, the lowest band at 1332 MHz was not used for the fit, since it may contain large uncertainties derived from the data at  $< 1.5$  GHz (shown in figure 1). We used the images made with the robustness  $r = 2.0$ , which was the one used to estimate the upper limit of diffuse emission in this paper. We find that the spectral index is  $\alpha_{\text{obs}} = 0.85$ , which implies that the source is likely an unresolved Fanaroff–Riley radio galaxy rather than a quasar with a flat spectral index. If this is the case, the slope could extend to lower frequency bands (e.g., Farnes et al. 2014). The extrapolation of the fit gives 129.76 mJy at 843 MHz and 562.88 mJy at 150 MHz, which are in agreement with 130.6 mJy at 843 MHz (SUMSS) and 573 mJy at 150 MHz (TGSS), respectively, on an error level of a few percent (figure 8). Therefore, we conclude that the flux scale of our observation is reasonable and our upper limit of diffuse emission is reliable. Note that we also performed such a comparison for images with different robustness and bandwidth, and obtained an uncertainty of typically  $\sim 10\%$ – $20\%$  on the flux scale.

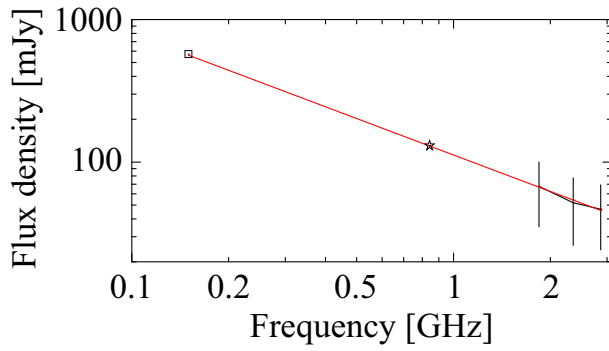


**Fig. 8.** Total intensity spectrum of SUMSS J140033–473800. The black solid line with error bars show the ATCA 512 MHz data with CA06 and  $r = 2.0$ . The square and star indicate the data of TGSS and SUMSS, respectively. The red line is the best fit of the ATCA 512 MHz data. (Color online)

## Appendix 2 Synchrotron radiation from cosmic-ray electrons

We summarize the derivation of non-thermal properties referred in this paper. A similar derivation can be seen in, for example, Govoni and Feretti (2004).

We consider that there are fresh CReS near a shock front and their energy spectrum follows a power law with an index  $p$ . We consider  $p > 2$  in order to avoid an imaginary Mach number in the DSA picture,  $M^2 = (p + 2)/(p - 2)$ . The number density of CReS between the Lorentz factor  $\gamma$  and  $\gamma + d\gamma$  is defined as

$$n_{ce}(\gamma)d\gamma = N_0\gamma^{-p}d\gamma, \quad (\text{A1})$$

where  $N_0$  is the normalization in units of  $\text{cm}^{-3}$ . The number density of CReS is given by integrating the equation,

$$\begin{aligned} n_{ce} &= N_0 \int_{\gamma_{\min}}^{\gamma_{\max}} \gamma^{-p} d\gamma \\ &\equiv N_0 N_1(p, \gamma_{\min}, \gamma_{\max}) (\text{cm}^{-3}) \end{aligned} \quad (\text{A2})$$

where  $N_1 = [\gamma^{1-p}]_{\gamma_{\min}}^{\gamma_{\max}} / (1 - p)$ . Likewise, the energy density of CReS can be calculated as

$$\begin{aligned} \varepsilon_{ce} &= N_0 m_e c^2 \int_{\gamma_{\min}}^{\gamma_{\max}} \gamma^{1-p} d\gamma \\ &\equiv N_0 m_e c^2 N_2(p, \gamma_{\min}, \gamma_{\max}) (\text{erg}/\text{cm}^3) \end{aligned} \quad (\text{A3})$$

where  $m_e$  is the electron rest mass,  $c$  is the speed of light, and  $N_2 = [\gamma^{2-p}]_{\gamma_{\min}}^{\gamma_{\max}} / (2 - p)$ .

While  $p$  is positive and steep,  $n_{ce}$  and  $\varepsilon_{ce}$  are insensitive to  $\gamma_{\max}$  and we choose  $\gamma_{\max} = 3000$ . Actually, they change only by a few percent as we vary  $\gamma_{\max}$  from 3000 to infinity in the case of  $p = 3$ . Meanwhile, they significantly depend on  $\gamma_{\min}$ . We choose  $\gamma_{\min} = 200$  as a representative value, because CReS with  $\gamma \sim 300$  have the longest cooling

timescale and could be a dominant component in a typical cluster environment (Sarazin 1999).

The CRe density can be constrained under the assumption that a radio emitter is in a simple minimum energy equipartition (see, e.g., Pfrommer & Enßlin 2004). That is, the energy density of magnetic field,  $\varepsilon_B$ , is equal to the energy density of relativistic particles:

$$f\varepsilon_{ce} \equiv \varepsilon_{ci} + \varepsilon_{ce} = \varepsilon_B, \quad (\text{A4})$$

where  $\varepsilon_{ci}$  is the energy density of cosmic-ray ions, and  $f$  is the cosmic-ray energy fraction;  $f = 2$  ( $\varepsilon_{ci}:\varepsilon_{ce} = 1:1$ ) for example. With this assumption, we obtain

$$N_0 = \frac{B^2}{8\pi f m_e c^2 N_2}. \quad (\text{A5})$$

$$n_{ce} = \frac{N_1 B^2}{8\pi f m_e c^2 N_2} \equiv N^*(p, \gamma_{\min}, \gamma_{\max}) B^2, \quad (\text{A6})$$

For example,  $N_0 \sim 1.0 \times 10^{-5} \text{ cm}^{-3}$  and  $N^* \sim 65 \text{ cm}^{-3} \text{ G}^2$ , if we consider  $(f, p, \gamma_{\min}, \gamma_{\max}) = (2, 3, 200, 3000)$ .

The synchrotron emissivity depends on the strength of the magnetic field perpendicular to the LOS,  $B_{\perp}$ . Specific Stokes parameters of synchrotron radiation can be written as (see Rybicki & Lightman 1979; Waelkens et al. 2009),

$$I = \int G_1(p) N_0(r) B_{\perp}(r)^{(1+p)/2} \omega^{(1-p)/2} dr, \quad (\text{A7})$$

$$Q + iU = \int G_2(p) N_0(r) B_{\perp}(r)^{(1+p)/2} \omega^{(1-p)/2} e^{2i\chi(r)} dr, \quad (\text{A8})$$

where  $\chi$  is the initial polarization angle at  $r$  and  $\omega = 2\pi\nu$  is the angular frequency. Other physical coefficients are  $G_1(p) = 2g_1(p)j(p)$ ,  $G_2(p) = 2g_2(p)j(p)$ ,

$$j(p) = \frac{1}{4\pi} \frac{\sqrt{3}e^3}{8\pi m_e c^2} \left( \frac{2m_e c}{3e} \right)^{(1-p)/2}, \quad (\text{A9})$$

$$g_1(p) = \frac{1}{1+p} 2^{(1+p)/2} \Gamma\left(\frac{p}{4} - \frac{1}{12}\right) \Gamma\left(\frac{p}{4} + \frac{19}{12}\right), \quad (\text{A10})$$

$$g_2(p) = 2^{(p-3)/2} \Gamma\left(\frac{p}{4} - \frac{1}{12}\right) \Gamma\left(\frac{p}{4} + \frac{7}{12}\right), \quad (\text{A11})$$

where  $e$  is the electric charge and  $\Gamma$  is the  $\Gamma$  function. For a uniform medium with the LOS depth  $D_{\text{los}}$ , equation (A7) is integrated as

$$I = \frac{G_1 D_{\text{los}}}{8\pi f m_e c^2 N_2} B_{\perp}^{(1+p)/2} B^2 \omega^{(1-p)/2}. \quad (\text{A12})$$

We adopt a simple case where a weak, pre-amplified intergalactic magnetic field is just compressed by the shock,

hence the component parallel to the shock normal is negligibly small. Considering the case that the shock normal is on the plane of the sky, the strength of the magnetic field perpendicular to the LOS is equal to the strength of the magnetic field parallel to the LOS. It means  $B = \sqrt{2}B_{\perp}$ . The intensity is written as

$$I = I^*(p, \gamma_{\min}, \gamma_{\max}) B^{(5+p)/2} \omega^{(1-p)/2} \\ = \frac{2^{-(1+p)/4} G_1 D_{\text{los}}}{8\pi f m_e c^2 N_2} B^{(5+p)/2} \omega^{(1-p)/2}. \quad (\text{A13})$$

The thermal energy density,  $\varepsilon_T$ , and  $\varepsilon_B$  are respectively given in  $\text{erg cm}^3$  by

$$\varepsilon_T = \frac{3}{2} nkT = 4.00 \times 10^{-12} \left( \frac{n_e}{10^{-3} \text{cm}^{-3}} \right) \left( \frac{T_e}{10^7 \text{K}} \right), \quad (\text{A14})$$

$$\varepsilon_B = \frac{B^2}{8\pi} = 3.98 \times 10^{-14} \left( \frac{B}{\mu\text{G}} \right)^2, \quad (\text{A15})$$

where  $n$  and  $T$  are the ICM density and temperature, respectively. The ICM is assumed to be in thermal equilibrium ( $T = T_e$ , where  $T_e$  is the electron temperature) and fully-ionized with the mass fractions of hydrogen  $X = 0.76$  and those of helium  $Y = 0.24$ . We can then estimate the energy budget of the non-thermal components under the energy equipartition:

$$\varepsilon_{NT} = \varepsilon_{\text{ci}} + \varepsilon_{\text{ce}} + \varepsilon_B = 2\varepsilon_B \quad (\text{A16})$$

$$\frac{\varepsilon_{NT}}{\varepsilon_T} < 1.99\% \left( \frac{B}{1 \mu\text{G}} \right)^2 \left( \frac{10^{-3} \text{cm}^{-3}}{n_e} \right) \left( \frac{10^7 \text{K}}{T_e} \right). \quad (\text{A17})$$

## References

- Akahori, T., & Yoshikawa, K. 2008, PASJ, 60, L19  
 Akahori, T., & Yoshikawa, K. 2010, PASJ, 62, 335  
 Akahori, T., & Yoshikawa, K. 2012, PASJ, 64, 12  
 Akamatsu, H., et al. 2016, A&A, 593, L7  
 Akamatsu, H., & Kawahara, H. 2013, PASJ, 65, 16  
 Blandford, R., & Eichler, D. 1987, Phys. Rep., 154, 1  
 Bock, D., Large, M. I., & Sadler, E. M. 1999, AJ, 117, 1578  
 Bonafede, A., et al. 2014, MNRAS, 444, L44  
 Brunetti, G., Cassano, R., Dolag, K., & Setti, G. 2009, A&A, 507, 661  
 Brunetti, G., Venturi, T., Dallacasa, D., Cassano, R., Dolag, K., Giacintucci, S., & Setti, G. 2007, ApJ, 670, L5  
 Caprioli, D., & Spitkovsky, A. 2014, ApJ, 783, 91  
 Carilli, C. L., & Taylor, G. B. 2002, ARA&A, 40, 319  
 Cassano, R., et al. 2013, ApJ, 777, 141  
 Cassano, R., Etori, S., Giacintucci, S., Brunetti, G., Markevitch, M., Venturi, T., & Gitti, M. 2010, ApJ, 721, L82  
 Dawson, W. A. 2013, ApJ, 772, 131  
 Dawson, W. A., et al. 2015, ApJ, 805, 143  
 de Gasperin, F., van Weeren, R. J., Brüggén, M., Vazza, F., Bonafede, A., & Intema, H. T. 2014, MNRAS, 444, 3130  
 Ebeling, H., Mullis, C. R., & Tully, R. B. 2002, ApJ, 580, 774  
 Enßlin, T., Pfrommer, C., Miniati, F., & Subramanian, K. 2011, A&A, 527, A99  
 Enßlin, T. A., Biermann, P. L., Klein, U., & Kohle, S. 1998, A&A, 332, 395  
 Farnes, J. S., Gaensler, B. M., & Carretti, E. 2014, ApJS, 212, 15  
 Feretti, L., Giovannini, G., Govoni, F., & Murgia, M. 2012, A&AR, 20, 54  
 Finoguenov, A., Sarazin, C. L., Nakazawa, K., Wik, D. R., & Clarke, T. E. 2010, ApJ, 715, 1143  
 Fujita, Y., Akamatsu, H., & Kimura, S. S. 2016, PASJ, 68, 34  
 Fujita, Y., Takizawa, M., Yamazaki, R., Akamatsu, H., & Ohno, H. 2015, ApJ, 815, 116  
 Fujita, Y., Tawa, N., Hayashida, K., Takizawa, M., Matsumoto, H., Okabe, N., & Reiprich, T. H. 2008, PASJ, 60, S343  
 Giovannini, G., Feretti, L., Girardi, M., Govoni, F., Murgia, M., Vacca, V., & Bagchi, J. 2011, A&A, 530, L5  
 Gitti, M., et al. 2015, in Advancing Astrophysics with the Square Kilometre Array, PoS (AASKA14) (Trieste: SISSA), 076  
 Govoni, F., & Feretti, L. 2004, Int. J. Mod. Phys. D, 13, 1549  
 Govoni, F., Murgia, M., Xu, H., Li, H., Norman, M. L., Feretti, L., Giovannini, G., & Vacca, V. 2013, A&A, 554, 102  
 Guo, X., Sironi, L., & Narayan, R. 2014, ApJ, 794, 153  
 Hurler-Walker, N., et al. 2017, MNRAS, 464, 1146  
 Intema, H. T., Jagannathan, P., Mooley, K. P., & Frail, D. A. 2017, A&A, 598, A78  
 Itahana, M., Takizawa, M., Akamatsu, H., Ohashi, T., Ishisaki, Y., Kawahara, H., & van Weeren, R. J. 2015, PASJ, 67, 113  
 Jee, M. J., Dawson, W. A., Stroe, A., Wittman, D., van Weeren, R. J., Brüggén, M., Bradač, M., & Röttgering, H. 2016, ApJ, 817, 179  
 Johnston-Hollitt, M., et al. 2015, in Advancing Astrophysics with the Square Kilometre Array, PoS (AASKA14) (Trieste: SISSA), 092  
 Kale, R., et al. 2015, A&A, 579, A92  
 Kang, H., & Ryu, D. 2013, ApJ, 764, 95  
 Kang, H., Ryu, D., & Jones, T. W. 2017, ApJ, 840, 42  
 Kato, Y., Nakazawa, K., Gu, L., Akahori, T., Takizawa, M., Fujita, Y., & Makishima, K. 2015, PASJ, 67, 71  
 Kitayama, T., et al. 2016, PASJ, 68, 88  
 Kocevski, D. D., Ebeling, H., Mullis, C. R., & Tully, R. B. 2007, ApJ, 662, 224  
 Markevitch, M., & Vikhlinin, A. 2007, Phys. Rep., 443, 1  
 Matsukiyo, S., Ohira, Y., Yamazaki, R., & Umeda, T. 2011, ApJ, 742, 47  
 Matsukiyo, S., & Matsumoto, Y. 2015, J. Phys. Conf. Ser., 642, 012017  
 Nakazawa, K., et al. 2009, PASJ, 61, 339  
 Ogrea, G. A., Brüggén, M., van Weeren, R. J., Röttgering, H., Croston, J. H., & Hoeft, M. 2013, MNRAS, 433, 812  
 Okabe, N., Akamatsu, H., Kakuwa, J., Fujita, Y., Zhang, Y., Tanaka, M., & Umetsu, K. 2015, PASJ, 67, 114  
 Okabe, N., Bourdin, H., Mazzotta, P., & Maurogordato, S. 2011, ApJ, 741, 116  
 Okabe, N., & Umetsu, K. 2008, PASJ, 60, 345

- Ozawa, T., et al. 2015, PASJ, 67, 110
- Pfrommer, C., & Enßlin, T. A. 2004, MNRAS, 352, 76
- Rudnick, L., & Lemmerman, J. 2009, ApJ, 697, 1341
- Rybicki, G. B., & Lightman, A. P. 1979, Radiation Processes in Astrophysics (New York: Wiley-Interscience)
- Ryu, D., Kang, H., Hallman, E., & Jones, T. W. 2003, ApJ, 593, 599
- Sarazin, C. L. 1986, Rev. Mod. Phys., 58, 1
- Sarazin, C. L. 1999, ApJ, 520, 529
- Sarazin, C. L. 2002, in L. Feretti et al., ed., Merging Processes in Galaxy Clusters, (Dordrecht: Kluwer Academic Publishers), 1
- Takizawa, M. 2008, ApJ, 687, 951
- Trasatti, M., Akamatsu, H., Lovisari, L., Klein, U., Bonafede, A., Brügger, M., Dallacasa, D., & Clarke, T. 2015, A&A, 575, A45
- van Weeren, R. J., et al. 2017, Nature Astron., 1, 0005
- Vazza, F., & Brügger, M. 2014, MNRAS, 437, 2291
- Waelkens, A., Jaffe, T., Reinecke, M., Kitaura, F. S., & Enßlin, T. A. 2009, A&A, 495, 697
- Wilson, W. E., et al. 2011, MNRAS, 416, 832
- Xu, H., et al. 2012, ApJ, 759, 40